Taxonomy of high-pressure vibration spectra of zincblende semiconductor alloys – The percolation model applied to $Cd_{1-x}Zn_xTe$

T. Alhaddad,[1] M.B. Shoker,[2,a)] O. Pagès,[1,b)] A. Polian,[3,4] V.J.B. Torres,[5] Y. Le Godec,[3,4] J.-P. Itié,[4] C. Bellin,[3] K. Béneut,[3] S. Diliberto,[6] S. Michel,[6] A. Marasek[7] and K. Strzałkowski[7]

[1] Université de Lorraine, LCP-A2MC, UR 201019679B, F-57000 Metz, France
[2] University of Luxembourg, Department of physics and materials science, 41 rue du Brill, 4422 Belvaux, Luxembourg
[3] Institut de Minéralogie, de Physique des Matériaux et de Cosmochimie, Sorbonne Université — UMR CNRS 7590, F-75005 Paris, France
[4] Synchrotron SOLEIL, L'Orme des Merisiers Saint-Aubin, BP 48 F-91192 Gif-sur-Yvette Cedex, France
[5] Departamento de Fisica and I3N, Universidade de Aveiro, 3810 – 193 Aveiro, Portugal
[6] Institut Jean Lamour, UMR CNRS 7198, Campus Artem, Université de Lorraine, 57078, Metz, France
[7] Institute of Physics, Faculty of Physics, Astronomy and Informatics, Nicolaus Copernicus University in Toruń, ul. Grudziądzka 5, 87-100 Toruń, Poland

Supplementary material

This annex reports on additional experimental, *ab initio* and theoretical data, besides those provided in the main text, further supporting the discussion of the $Cd_{1-x}Zn_xTe$ lattice structure/dynamics depending on pressure across the composition domain. In preamble to such fundamental issues, we briefly discuss in **Sec. SI** (prefix S stands for supplementary material) novel applications opened by the percolation model (PM). In **Sec. SII** we focus on the lattice relaxation/structure studied by high-pressure X-ray diffraction (HP-XRD) at the PSICHÉ beamline of SOLEIL synchrotron. Selected raw HP-diffractograms taken at large and small Cd contents inform on the pressure dependence of the lattice parameter of the zincblende phase (**Sec. SII.1**), from which is deduced the bulk modulus at ambient pressure B_0 – via a fitting of the pressure (P) dependence of the unit cell volume to a Birch-Murnaghan equation of state (**Sec. SII.2**). This provides an insight into the $Cd_{1-x}Zn_xTe$ mechanical properties in bulk. A complementary insight into the bond-related $Cd_{1-x}Zn_xTe$ mechanical properties is obtained in **Sec. SIII** by addressing the lattice dynamics using high-pressure Raman scattering (HP-RS). Experimental and/or *ab initio* TO and LO data are separately treated using the same model of two coupled harmonic (mass + restoring force) oscillators rolled out through suitable TO (**Sec. SIII.1**) and LO (**Sec. SIII.2**) approaches, and eventually compared in **Sec. SIII.3** in which we briefly outline a refined TO treatment beyond that reported in the main text.

[a)] This research was performed while M.B. Shoker was doing his PhD at Laboratory LCP-A2MC (affiliation 1).
[b)] Author to whom correspondence and requests for materials should be addressed: olivier.pages@univ-lorraine.fr

I. PM applications

From a practical point of view there are two main topics of interest related to the PM.

First, the PM offers a suitable platform to discuss the dispersion relation and lifetimes of the phonon-polaritons propagating in bulk of cubic and hexagonal semiconductor alloys (SCA). Such phonon/photon-coupled modes remained unexplored experimentally until our pioneering near-forward Raman studies[S1]. Interestingly alloying generates a special phonon-polariton (not paralleled in the pristine compounds) that remains supported by the crystal across most of its dispersion and that gains lifetime on acquiring high (photon-like) velocities[S2]. Such phonon-polariton bridges from lattice dynamics towards photonics, as an option to ultimately accelerate the signal processing in matter in the THz range.

Second, the sensitivity of bond vibrations to their "same" or "alien" environments formalized within the PM can be exploited to judge whether the A↔B substitution proceeds randomly or by causing clustering/anticlustering. A quantitative insight at a given composition is obtained by comparing the relative Raman intensities of the various submodes forming the PM-multiplet due to a given bond. This was tested on cubic diamond Ge_xSi_{1-x}[S3] and on zincblende $Zn_{1-x}Be_xSe$[S4] and $Cd_{1-x}Zn_xSe$[S5], with *ab initio* Raman/phonon calculations in support. The historical models fail to address the raised issue, either by construction (the MREI model is blind to the alloy disorder) or due to a certain ambiguity of the model (cluster model)[16]. The latter ambiguity relates to the 1D vs. 3D ambivalence of the cluster model in that the individual oscillators behind the Raman modes are identified at three-dimension (3D, referring to tetrahedron-cluster units – see main text) whereas the equations of motion per bond are scalar, *i.e.*, defined at one-dimension (1D) along the linear chain approximation. More detail is given in Refs.[10,16]. Solid-state nuclear magnetic resonance[29] as well as extended X-ray absorption fine structure measurements of the next-nearest-neighbor bond length[S6] are also capable of elucidating the nature of the A↔B substitution. In comparison, Raman scattering is non-destructive, fast and easy to perform.

II. High-pressure X-ray diffraction

II.1. Experiment

A selection of raw $Cd_{1-x}Zn_xTe$ HP-diffractograms obtained at moderate (x=0.28) and large (x=0.89) Zn contents in the upstroke at the PSICHÉ beamline of SOLEIL synchrotron using the 0.3738 Å radiation is displayed in Figs. S1a and S1b, respectively. Sharp peaks are observed at any composition and pressure, the sign of a high crystal quality. The individual peaks are labeled according to their (hkl) Miller's indices in the relevant crystal phases, abbreviated zb (zincblende), cb (cinnabar), rs (rock-salt) and cm (Cmcm). The selected diffractograms emphasize the sensitive pressure domains corresponding to pure crystal phases (hollow symbols) and to phase coexistence (filled symbols).

II.2. Bulk modulus

Figs. 2a and 2b display the P-dependence of lattice parameter(s) of $Cd_{0.72}Zn_{0.28}Te$ and $Cd_{0.09}Zn_{0.91}Te$ deduced from HP-XRD diffractograms, partly displayed in Fig. S1a and S1b. The corresponding unit cell volume vs. P in the zincblende phases are fitted to the Birch-Murnaghan equation of state (curves) in Fig. S2a[40]. The unit cell volume of the zincblende phase at 0 GPa enters into the fit as a sensitive input parameter. This is estimated from the lattice parameter (a) measured at ambient conditions using the Cu Kα line. Such XRD data (examples of diffractograms are shown in Ref.[31]) reveal a linear a vs. x variation across the series of zincblende $Cd_{1-x}Zn_xTe$ single crystals (Fig. S2b, filled circles) in line with the parent values taken from the literature (hollow circles)[41]. This is consistent with current *ab initio* calculations done on large disordered $Cd_{1-x}Zn_xTe$ supercells across the composition domain (squares). The alloy-related XRD data are marred by error bars representing uncertainty in the x estimate by the induced coupling plasma method. The B_0 and B_0' values resulting from the fit are discussed in the main text (Fig. 2c).

III. High-pressure Raman scattering

HP-RS experiments are performed at symmetric compositions at both ends of the $Cd_{1-x}Zn_xTe$ composition domain, *i.e.*, with $Cd_{0.89}Zn_{0.11}Te$ (x~0.1), on the one hand, in search for the LO modes, and with $Cd_{0.09}Zn_{0.91}Te$ and $Cd_{0.13}Zn_{0.87}Te$ (x~0.9), on the other hand, focusing on the TO modes.

III.1. HP-RS on TO modes

III.1.a. Experiment (x~0.9)

Unpolarized high-pressure Raman spectra taken with the 632.8 nm laser line at 300 K across the zincblende phases of $Cd_{0.09}Zn_{0.91}Te$ and $Cd_{0.13}Zn_{0.87}Te$ (0 – 9 GPa) in the upstroke (full lines) and in the downstroke (dotted line) are shown in Figs. S3a and S3b, respectively. The TO inversion in the upstroke (○↔●) discussed in the main text around Figs. 3a and 3b is sequenced step-by-step for the first crystal, and verified for the second one.

At ambient pressure, the Zn-Te TO submodes (□ and ■) are presumably decoupled (see main text), and hence labeled with a subscript and a superscript specifying the bond vibration and the local environment ("same" or "alien"). When the two TO submodes are forced to proximity by pressure, they do mechanically couple, rendering the above bond/environment-specific assignment obsolete. The neutral TO^- and TO^+ notation is then used in the main text, in order of increasing frequency. Simplicity is likewise retained for labeling, on the one hand, the main LO feature essentially due to the dominant Zn-Te bond, hence noted LO_{Zn-Te}, and, on the other hand, the CdTe-like impurity mode with degenerate TO-LO character at the studied minor Cd content – identified as O_{Cd-Te}, keeping "O" as main label to specify the optic character and omitting the T/L-prefix.

III.1.b. *Ab initio* calculations

- x~$x_{Cd-Te,perco}$ (0.81)

As discussed in the main text around Fig. S4, $Cd_{1-x}Zn_xTe$ develops a moderate version of scenario ① at $x \leq x_{Cd-Te,perco}$ in that the lower/dominant TO^{Zn}_{Zn-Te} does not freeze on crossing the upper/minor TO^{Cd}_{Zn-Te}. We can see one circumstantial reason and one intrinsic reason for this. First, Cd-Te and Zn-Te vibrate at nearly identical frequencies (recall the high-intricacy of the $Cd_{1-x}Zn_xTe$ phonon pattern[31]) – the circumstantial reason: the CdTe and ZnTe TO-LO bands are separated by less than ~5 cm^{-1}. Second, in the percolation regime ($x_{Zn-Te,perco} = 0.19 \leq x \leq x_{Cd-Te,perco} = 0.81$) the "alien" and "host environments" for Zn-Te are finely interlaced (as treelike continua[2]) – the intrinsic reason. Hence, the "alien" and "same" environments behind the two Zn-Te submodes cannot be distinguished at the resonance/crossing, either by their dynamics (due to the phonon intricacy) or by their spatial separation (due to the interlacing). In this case (frequency and spatial barriers unset) the two submodes merge into a unique/collective Zn-Te mode from their crossing/resonance onwards.

In the earlier tested zb-SCA listed above, the parent TO-LO bands are well-separated, by at least 40 cm^{-1} ($ZnSe_{1-x}S_x$[49]). The set frequency barrier between the "same" and "alien" environments of a given bond prevents the formation of a collective mode at the crossing/resonance in the percolation regime – despite the spatial barrier is unset (interlacing). In this case, the strict scenario ① applies, with freezing at the crossing[27].

At $x > x_{Cd-Te,perco}$, the "alien" and "same" environments of Zn-Te in $Cd_{1-x}Zn_xTe$ are spatially separated, resembling a dispersion in a swisscheese-like matrix[2]. The established spatial/topological barrier preserves the individual Zn-Te submodes originating from such environments across the convergence process – despite the frequency barrier being unset, until crossing at the resonance and switching post resonance (scenario ②).

- x~(0,1)

In this Sec. we study *ab initio* the pressure dependence of the $TO^{Zn}_{Zn-Te} - TO^{Cd}_{Zn-Te}$ Raman doublet of $Cd_{1-x}Zn_xTe$ at large Cd-dilution (x~1, Fig. S5a) and at large Zn-dilution (x~0, Fig. S5b) to complete the

same study done around the Cd-Te bond percolation threshold (x_{Cd-Te}=0.81, Fig. S4) in the main text. We use large (216-atom) zincblende-type CdTe- and ZnTe-like supercells containing minimal impurity motifs, *i.e.*, a Zn-trio (x~0) and a Cd-duo bridged by Te (x~1), noted CdTe:3Zn and ZnTe:2Cd, respectively. CdTe:3Zn notably provides the matrix-like TO_{Cd-Te} (oval, Fig. S5b) and TO_{Zn-Te} impurity (taken at the center of the dashed area) frequencies at 0 and 5 GPa, used to support the discussion of the LO^- and LO^+ modes of $Cd_{0.89}Zn_{0.11}Te$ (Fig. 3d) in the main text. In the following, the focus is on the impurity modes of CdTe:3Zn and ZnTe:2Cd.

At x~0 (CdTe:3Zn supercell, Figs. S4b) a trio of aligned Zn impurities suffices to generate two percolation-type Raman doublets, *i.e.*, one per spectral range. In the Zn-Te spectral range, a Zn-Trio is ideal to render the sensitivity of Zn-Te vibrations up to second-neighbors[31]. Out of the nine modes supported by the Zn-trio (due to three degrees of freedom per Zn), one vibrates in-chain and the remaining eight vibrate out-of-chain. The former is assigned in terms of Zn-Te vibrations in "same" environment (TO^{Zn}_{Zn-Te}, solid arrow) while the latter refer to the "alien" (TO^{Cd}_{Zn-Te}, the out-of-chain frequency domain is shaded in grey) environment, respectively. In the Cd-Te spectral range, the Zn-trio creates a local tension because the bond length is shorter for Zn-Te than for Cd-Te[26,31]. This gives rise to a local/minor Cd-Te vibration in presence of the "alien" Zn-trio (TO^{Zn}_{Cd-Te}, dotted arrow) at a lower frequency than the dominant Cd-Te vibrations in the "same" matrix-like environment away from the Zn-trio (TO^{Cd}_{Cd-Te}, oval). We are mainly interested in the pressure dependence of the $TO^{Zn}_{Zn-Te} - TO^{Cd}_{Zn-Te}$ doublet in the Zn-Te spectral range – in relation to Fig. 3a. However, a side comparison with the $TO^{Zn}_{Cd-Te} - TO^{Cd}_{Cd-Te}$ doublet in the Cd-Te spectral range is instructive.

As already mentioned (main text), the ZnTe-like environment hardens at a faster rate than the CdTe-like one under pressure. Accordingly, for a given bond species the pressure-induced upward shift is larger for the submode stemming from the former environment than for the submode due to the latter environment. This is especially clear for the Cd-Te doublet, to such extent that the original $TO^{Zn}_{Cd-Te} - TO^{Cd}_{Cd-Te}$ at 0 GPa is inverted at 7.5 GPa (as emphasized by a curved arrow in Fig. S5b), conforming to convergence scenario ②. The used CdTe-like supercell becomes unstable beyond 7.5 GPa – as observed in Ref.[21] (Fig. S7 therein), fixing the limit for the current *ab initio* study at x~0. The trend is similar in the Zn-Te spectral range, except that TO^{Zn}_{Zn-Te} (solid arrow) does not cross TO^{Cd}_{Zn-Te} but goes parallel with it at a fixed position from 5 GPa onwards. We emphasize that even at maximum pressure TO^{Zn}_{Zn-Te} fails to shift away from the TO^{Cd}_{Zn-Te} spectral range (shaded area), remaining strictly inside it. This manifests a moderate version of the convergence scenario ① as described in the main text around x_{Cd-Te}.

At x~1 (ZnTe:2Cd supercell, Fig. S5a), we focus on the $TO^{Zn}_{Zn-Te} - TO^{Cd}_{Zn-Te}$ doublet, of main interest. In this case, a mere Cd-duo of impurity (even an isolated Cd-impurity would suffice) helps to fix ideas. The Cd-duo generates a local strain in ZnTe, giving rise to a local/minor TO^{Cd}_{Zn-Te} mode at higher frequency than the dominant TO^{Zn}_{Zn-Te} one due to Zn-Te vibrations away from Cd. As expected, the (TO^{Zn}_{Zn-Te}, TO^{Cd}_{Zn-Te}) suffers an inversion under pressure (curved arrow in Fig. S5a), following the convergence scenario ②.

Summarizing, the CdTe:3Zn (x~0) and ZnTe:2Cd (x~1) *ab initio* insights reveal different convergence paths for the bimodal Zn-Te Raman signal of $Cd_{1-x}Zn_xTe$ in the (Cd,Zn)-dilute limits, *i.e.*, either the achievement of a phonon exceptional point at the resonance manifesting the interruption of crossing (through a moderate version of scenario ①, as detailed in the main text) or an effective crossing mediated by a free mechanical coupling of oscillators across the resonance eventually leading to a doublet inversion post resonance (scenario ②), respectively. Hence, scenarios ① and ② are inherent to Zn-Te bonds dispersed in chain ($x < x_{Cd-Te}$) and to matrix-like Zn-Te bonds ($x \geq x_{Cd-Te}$), respectively. This emphasizes a pivotal role of the Cd-Te bond percolation threshold ($x \geq x_{Cd-Te}$) regarding the scenario ① ↔ scenario ② transition, as discussed in the main text around Fig. S4.

III.2. HP-RS on LO modes (x~0.1)

The experimental HP-RS LO study of $Cd_{0.89}Zn_{0.11}Te$ is achieved in near resonant conditions with the 488.0 nm laser excitation operated at 77K. A reference $Cd_{0.89}Be_{0.11}Te$ sample placed in the same pressure chamber of the DAC (inset of Fig. S6) is used for *in situ* calibration of the available Cd-Te oscillator strength across the studied pressure domain (see below). Somewhat fortuitously, the two samples have exactly the same composition within a half percent. Hence, the amount of Cd-Te oscillator strength found with $Cd_{0.89}Be_{0.11}Te$ at a given pressure can be used as such for $Cd_{0.89}Zn_{0.11}Te$ (being clear that a difference in alloy composition would not have been problematic, anyway). Another fortuitous analogy between $Cd_{0.89}Be_{0.11}Te$ and $Cd_{0.89}Zn_{0.11}Te$ is that they transite from zincblende to rock-salt at the same critical pressure, *i.e.*, ~5.5 GPa (within experimental resolution), referring to existing HP-XRD data in the literature at nearly ($Cd_{0.93}Be_{0.07}Te$ – Ref.[21]) or exactly the same ($Cd_{0.89}Zn_{0.11}Te$ – Ref.[37]) Cd-compositions.

The series of LO-like Raman spectra jointly taken with $Cd_{0.89}Zn_{0.11}Te$ (thick lines) and $Cd_{0.89}Be_{0.11}Te$ (thin lines) in the upstroke across the pressure range of their zincblende phases are reported in Fig. S6.

The TO_{Be-Te} and LO_{Be-Te} modes of $Cd_{0.89}Be_{0.11}Te$ are quasi degenerated due to the minor Be content[21], hence regrouped without distinction under the common O_{Be-Te} label – omitting the T/L-prefix. Be-Te is most covalent-stiff/light among II-VI's[26,39], which generates a Be-Te Raman signal at much higher frequency, *i.e.*, around 400 cm^{-1}, than that due to the comparatively ionic-soft/heavy Cd-Te matrix-like bonds, showing up around 175 cm^{-1}. The LO_{Cd-Te} and LO_{Be-Te} modes of $Cd_{0.89}Be_{0.11}Te$ are thus well-separated and thus electrically decoupled – the reason why they can be assigned to specific bonds (subscript). This offers the possibility to measure *in situ* the pressure dependence of the parent CdTe oscillator strength (see methods), to be re-used for modeling of the complex $Cd_{0.89}Zn_{0.11}Te$ LO Raman signal (see main text).

The lower/dominant matrix-like LO_{Cd-Te} and upper/minor impurity-like LO_{Zn-Te} of $Cd_{0.89}Zn_{0.11}Te$ show up nearby at ambient pressure (0 GPa) and hence couple via their common macroscopic LO-like electric field E. This results in a pair of E-coupled LO^- (●) and LO^+ (○) modes with similar intensities, ranked in order of frequency[31]. As apparent in Figs. 3c/d and S6, LO^- diverges from LO^+ and reinforces at the expense of LO^+ in the upstroke, two signs of E-decoupling. Basically, by increasing pressure the bare-uncoupled LO_{Cd-Te} and LO_{Zn-Te} behind the E-coupled LO^- and LO^+ break away, which detunes the resonance. With this, LO^- and LO^+ tend to decouple and the $LO^- \rightarrow LO^+$ transfer of oscillator strength mediated by $\vec{E}$-coupling is progressively suppressed, until (ideally) the natural intensity balance between the lower/dominant (matrix-like) LO_{Cd-Te} and upper/minor (impurity-like) LO_{Zn-Te} is eventually restored. Both the divergence (frequency aspect – bright curves) and the reversed transfer of oscillator strength (intensity aspect – brightness of curves) between LO^+ and LO^- are fairly reproduced theoretically in Figs. 3c/d, as discussed in the main text. Additional theoretical insight into the Raman intensity balance between LO^- and LO^+ at maximum pressure is provided in Fig. S6 (thick curve, shifted beneath the experimental spectrum).

III.3. TO (x~0.9) vs. LO (x~0.1) comparison

The amount of hybridization and strength of coupling between Raman modes near the resonance are compared in the TO (x~0.9 – Fig. 3e) and LO (x~0.1, Fig. 3f) cases using the same model of two coupled harmonic oscillators. Only, the nature of oscillators changes with the phonon symmetry, as extensively discussed, *e.g.*, in Ref.[13], and briefly recalled hereafter.

Due to the quasi vertical dispersion of the laser excitation, Raman scattering operates at long wavelength, justifying a common description of TO and LO Raman modes in terms of macroscopic excitations. In the used backscattering Raman setup, the magnitude q of the transferred wavevector is maximum, of the order of 1% of the Brillouin zone size. This is much larger, by two orders of magnitude, than the q value of a pure macroscopic transverse electric field, *i.e.*, a photon, propagating at THz (phonon-like) frequencies. Hence the transverse electric field E_T which is likely to accompany the TO modes of a polar crystal (such as a zincblende-type one) cannot propagate, in fact. Hence, the

TO detected in a backscattering Raman experiment is non-polar, *i.e.*, deprived of macroscopic electric field (E_T=0)[13]. It reduces to a purely mechanical ("mass + spring") harmonic oscillator. Such crude terminology is retained throughout this work for clarity/convenience being clear that the "spring-like" restoring force of such TO oscillator is not strictly "mechanical" (it only comes as such in the model), but involves the polarity of the chemical bond via the charges and polarizabilities of the anion and cation. The exact expression of the "mechanical" restoring force, given in Ref.[3], is obtained by operating the Lorentz's correction to the local electric field when adopting a description of a Raman mode in terms of its accompanying macroscopic (q~0) electric field. In contrast, the polar character is preserved for a LO oscillator ($E_L \neq 0$). This is because its macroscopic electric field E_L being longitudinal in character is not subject to any photon-like restriction. A LO harmonic oscillator thus involves a Coulombian (electrical) restoring force besides the spring-like (mechanical) one that solely governs a TO harmonic oscillator[13].

The following is an addendum to the TO vs. LO comparison done in the main text, reporting on a variant of the TO treatment. The same basic set of equations is used to describe the TO and LO oscillators, given by Eq. 4 of Ref.[28] (after taking out the generalized forces – see main text). This includes one equation of motion (bond-stretching) per oscillator, involving mechanical (spring-like) and electrical (Coulombian) restoring forces, plus an overall polarization equation used to specify the TO ($\varepsilon_r \to \infty$) or LO ($\varepsilon_r = 0$) character of the oscillators. The latter equation primarily involves the macroscopic electric field E due to the bond ionicity, governed by the relative dielectric function ε_r of the crystal – as specified in brackets above. We emphasize that in the used equation set, the fraction of a given oscillator in the crystal merely appears through the polarization equation. This information disappears for the purely-mechanical TO modes (see methods) probed in the used backscattering geometry[13], meaning that all TO oscillators are treated with equal weight in this case, by default.

Strictly, such TO approach makes sense only if both oscillators are equally represented in the crystal, as in the case of $Zn_{0.5}Be_{0.5}Se$[27] (treated in line with the approach developed by Dolfo and Vigué[S7]). This is not so in the present $Cd_{0.11}Zn_{0.89}Te$ case, in which one oscillator is dominant (TO^{Zn}_{Zn-Te}) and the other minor (TO^{Cd}_{Zn-Te}). This justifies a more refined approach to weight the mechanical coupling suffered by a given (u_i) oscillator by the fraction (x_j) of the other (u_j) oscillator in the crystal. By doing so, the dynamical matrix $\widetilde{M}_T$ related to the TO modes turns asymmetric, so that the net coupling efficiency ($\sqrt{V_{12}V_{21}}/\Delta$) involves the geometrical means of the off-diagonal $\widetilde{M}_T$-terms. However, this asymmetric (x-dependent) case generates few changes in the pressure dependence of the net coupling efficiency with respect to the symmetric (x-independent) case, as apparent in Fig. S7.

Supplementary material – only references

[S1] Hajj Hussein, R., Pagès, O., Firszt, F., Paszkowicz, W. & Maillard A. Near-forward Raman scattering by bulk and surface phonon-polaritons in the model percolation-type ZnBeSe alloy. *Appl. Phys. Lett*. **103**, 071912 (2013).

[S2] Dicko, H., Pagès, O., Shoker, M.B., Firszt, Strzałkowski, K., Maillard, A., Polian, A., Battie, Y., Broch, L., En Naciri, A., Postnikov, A.V., Paszkowicz, W. & Itié, J.P. Defect-induced ultimately fast volume phonon-polaritons in the wurtzite Zn0.74Mg0.26Se mixed crystal. *Sci. Rep.* **9**, 7817 (2019).

[S3] Torres, V.J.B., Hajj Hussein, R., Pagès, O. & Rayson, M.J. Clustering/anticlustering effects on the GeSi Raman spectra at moderate (Ge,Si) contents: Percolation scheme vs. *ab initio* calculations. *J. Appl. Phys.* **121**, 085704 (2017).

[S4] Pagès, O. *et al*. Non-random Be-to-Zn substitution in ZnBeSe alloys: Raman scattering and *ab initio* calculations. *Eur. Phys. J. B* **73**, 461–469 (2010).

[S5] Shoker, M.B. *et al*. Multi-phonon (percolation) behavior and local clustering of $Cd_xZn_{1-x}Se$-cubic mixed crystals ($x \leq 0.3$): A Raman-*ab initio* study. *J. Appl. Phys*. **126**, 105707 (2019).

[S6] Schnohr, C.S. Compound semiconductor alloys rom atomic scale structure to band gap bowing. *Appl. Phys. Rev*. **2**, 031304 (2015).

[S7] G. Dolfo, and J. Vigué, "Damping of coupled harmonic oscillators," *Eur. J. Phys.* **39**, 025005 (2018).

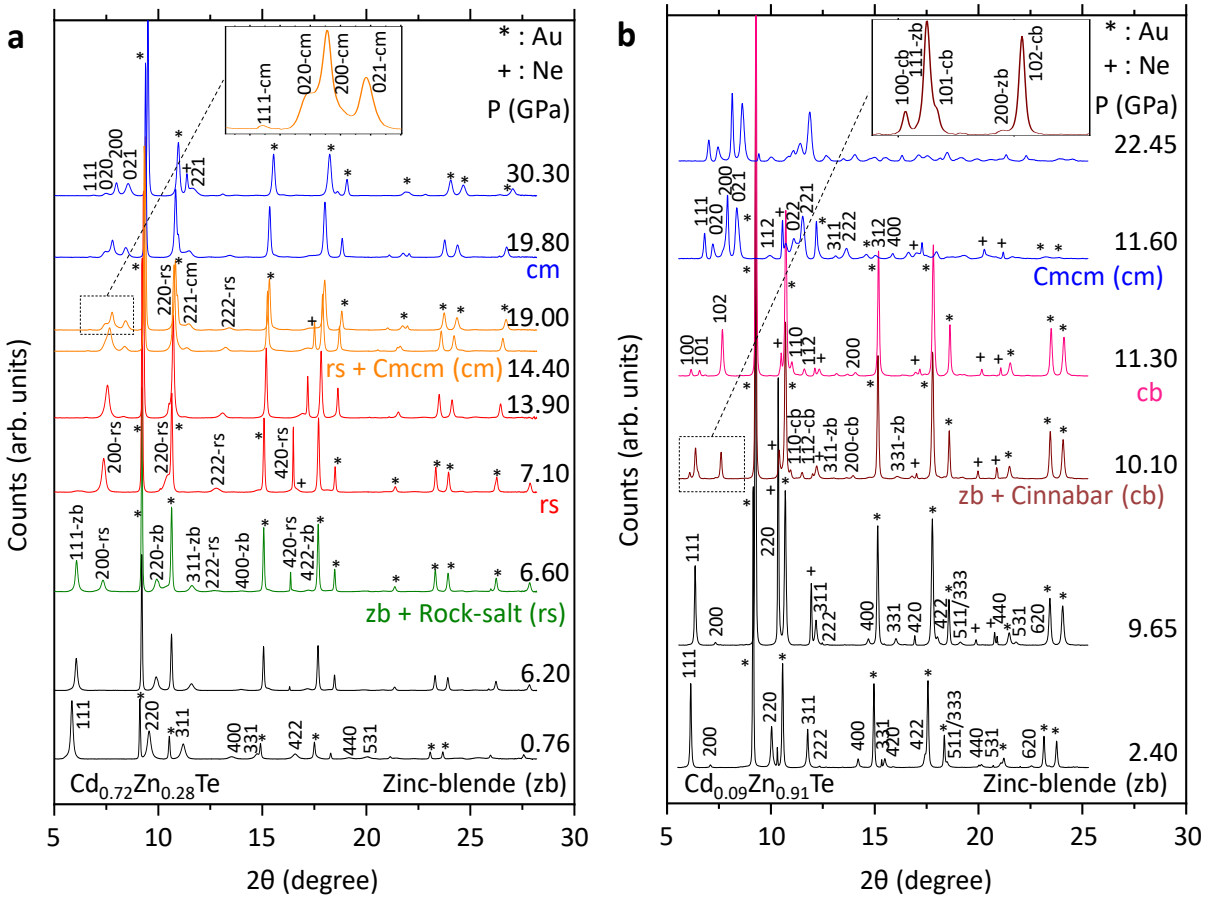

284

285 **FIG. S1**: **High-pressure $Cd_{1-x}Zn_xTe$ X-ray diffractograms.** Selected **(a)** $Cd_{0.72}Zn_{0.28}Te$ and **(b)** $Cd_{0.09}Zn_{0.91}Te$ powder
286 HP-XRD diffractograms taken in the upstroke with special attention to the pure-phase and mixed-phase domains.
287 The individual peaks are labelled using the (hkl) Miller indices of diffraction planes in various (zincblende-zb,
288 cinnabar-cb, rock-salt-rs, Cmcm-cm) phases, distinguished by using a color code (also used in Fig. 2). Additional
289 diffraction peaks originate from Au and Ne used for pressure calibration and as the pressure transmitting
290 medium, respectively, as indicated.

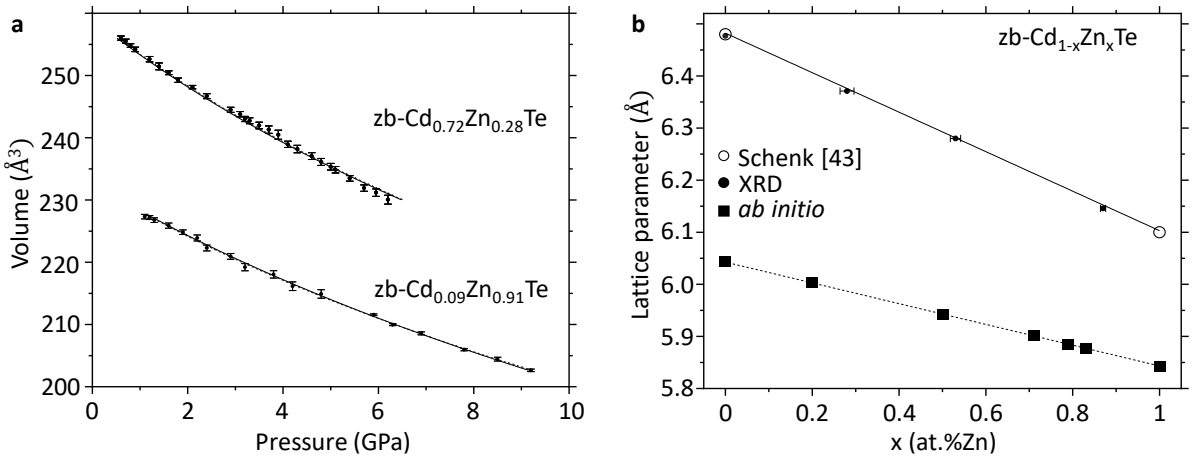

Fig. S2: **Structural parameters of zincblende-$Cd_{1-x}Zn_xTe$ depending on composition/pressure. (a)** Unit cell volume vs. pressure dependence of $Cd_{1-x}Zn_xTe$ (x=0.28, 0.91) in the zincblende (zb) phase measured by powder HP-XRD (symbols) fitted to the Birch-Murnaghan equation of state (curves). The resulting B_0 and B_0' values are displayed in Fig. 1. **(b)** Experimental (circles) and predicted *ab initio* (squares, AIMPRO calculations) x-dependences of the lattice constant at ambient pressure. A linear trend between experimental parent values taken from the literature (solid line) is replicated in *ab initio* data (dotted line).

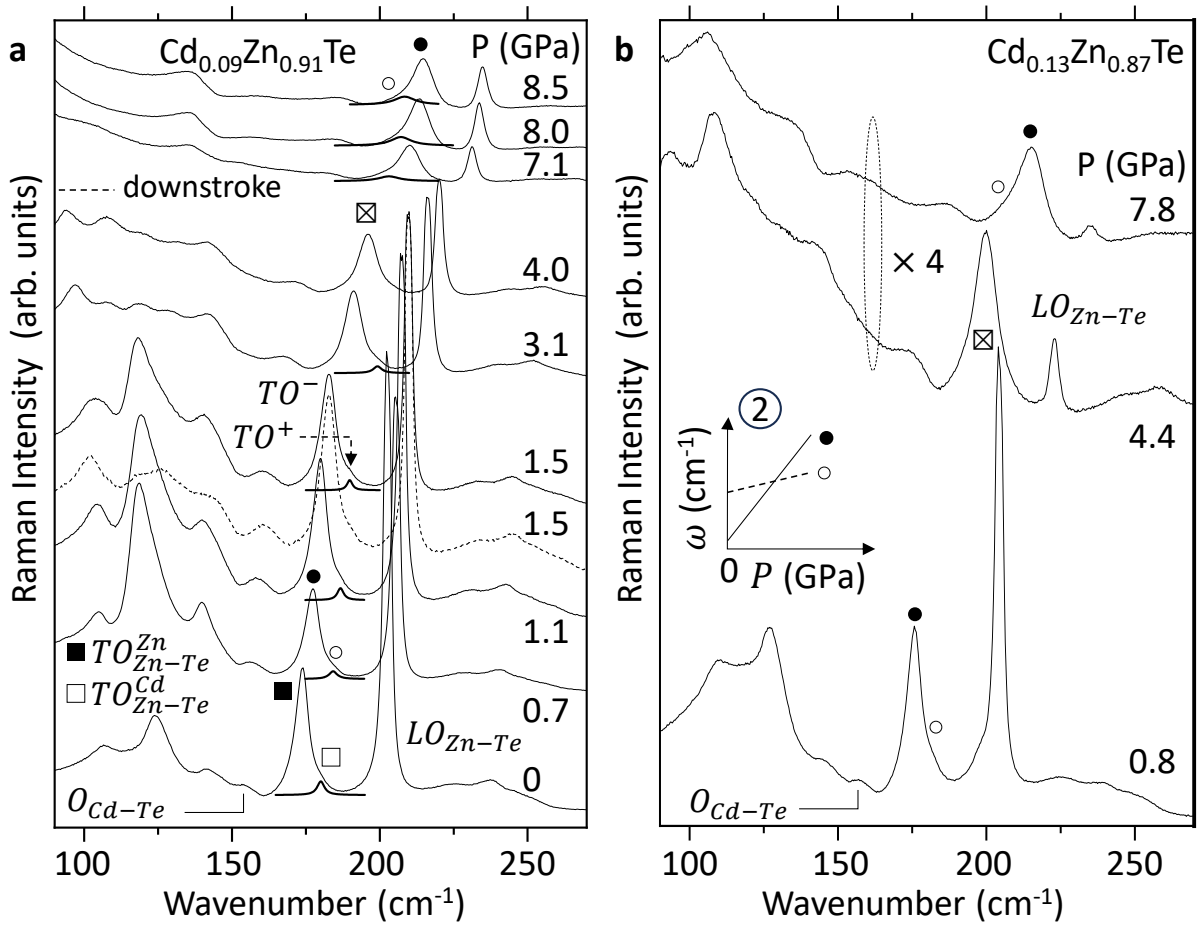

Fig. S3: **High-pressure $Cd_{1-x}Zn_xTe$ TO Raman spectra (x~0.9)**. High-pressure Raman spectra taken across the zincblende phase of **(a)** $Cd_{0.09}Zn_{0.91}Te$ and **(b)** $Cd_{0.13}Zn_{0.87}Te$ in the upstroke (solid curves) and downstroke (dotted curve). The dominant/matrix-like TO^{Zn}_{Zn-Te} (■) and minor/local TO^{Cd}_{Zn-Te} (□) bare–uncoupled modes at ambient pressure are forced to proximity in the upstroke and couple into related dominant (●) and minor (○, emphasized) modes with a crossing point around 4 GPa (⊠). This manifests the convergence scenario ② (inset). O_{Cd-Te} marks the quasi-degenerate $TO_{Cd-Te} - LO_{Cd-Te}$ mode.

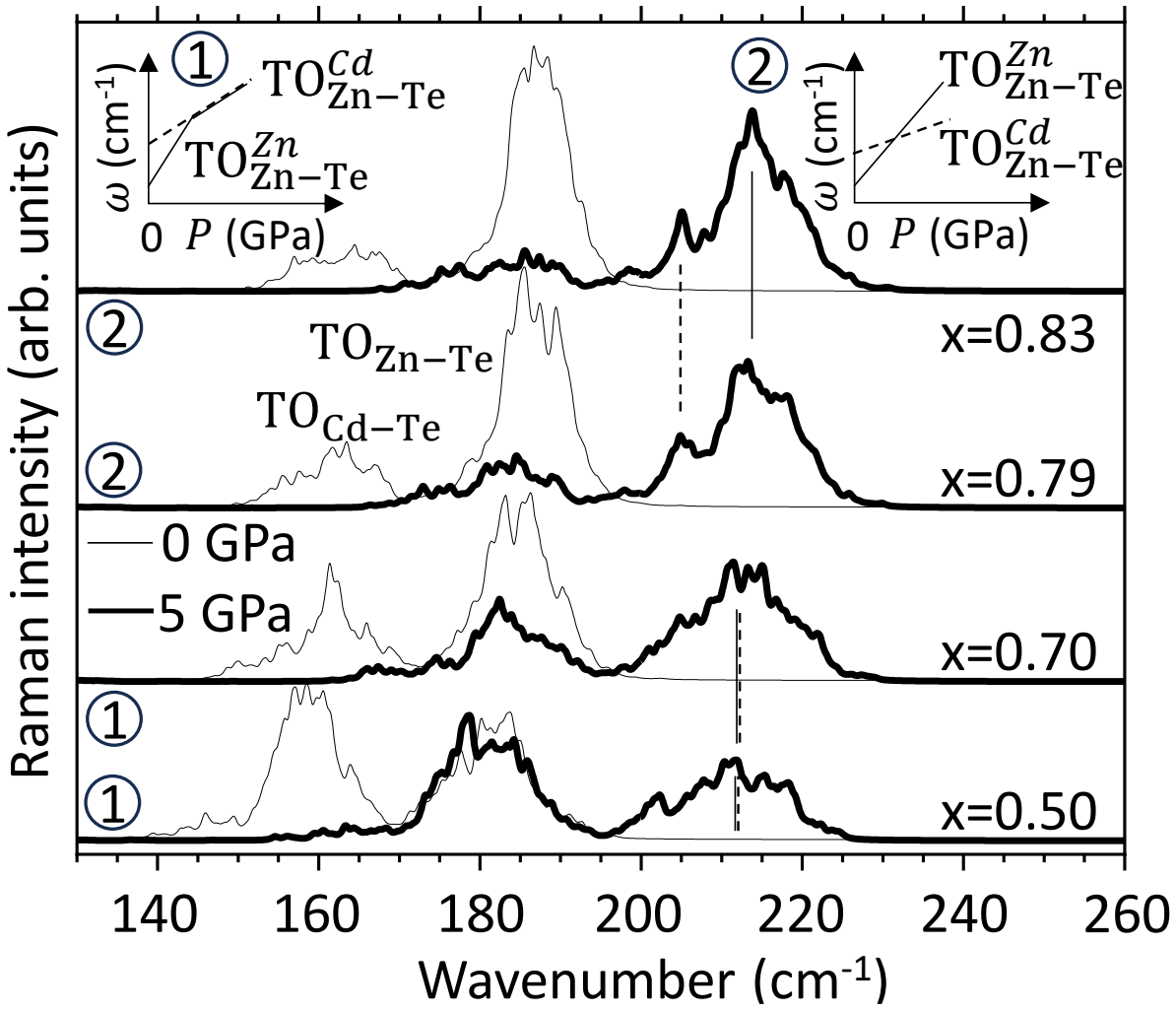

Fig. S4: ***Ab initio* high-pressure $Cd_{1-x}Zn_xTe$ TO Raman spectra at large Zn content.** *Ab initio* $Cd_{1-x}Zn_xTe$ high-pressure TO Raman spectra calculated on large (216-atom) disordered zincblende-supercells at various x values, as specified. Around the Cd-Te bond percolation threshold ($x_{Cd-Te,perco}$=0.81), the emergence of a minor feature (dotted line) on the low-frequency tail of the dominant Zn-Te feature (solid line) at high pressure suggests an inversion of the PM-type bimodal $TO^{Zn}_{Zn-Te} - TO^{Cd}_{Zn-Te}$ doublet when the Zn-Te bond is matrix-like ($x \geq x_{Cd-Te}$), in line with scenario ② (right inset). The minor feature disappears when Zn-Te is dispersed in chains ($x \leq x_{Cd-Te}$), suggesting the degeneracy of the two submodes from the resonance onwards, in line with scenario ① (left inset).

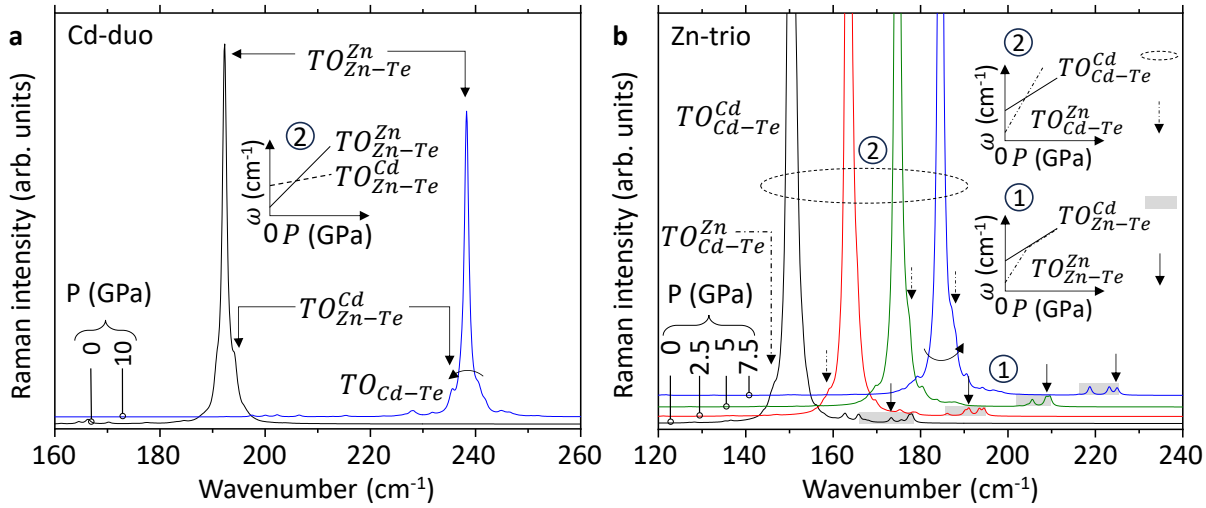

Fig. S5: ***Ab initio* high-pressure $Cd_{1-x}Zn_xTe$ TO Raman spectra at x~(0,1).** *Ab initio* pressure dependence of the TO^{Zn}_{Zn-Te} – TO^{Cd}_{Zn-Te} Raman doublet of zincblende-$Cd_{1-x}Zn_xTe$ in the **(a)** Cd-dilute (x~1, ZnTe:2Cd) limit and **(b)** Zn-dilute (x~0, CdTe:3Zn) limit. At x~1, the doublet refers to Zn-Te vibrations away from the Cd-duo, *i.e.*, matrix-like TO^{Zn}_{Zn-Te} (dominant feature), and close to it, in form of a local (minor) TO^{Cd}_{Zn-Te} mode, correspondingly. At x~0 the same doublet distinguishes between the in-chain (solid arrow) and out-of-chain (eight variants in total, regrouped under a dashed area) vibrations of the Zn-trio. The Zn-Te bimodal signal exhibits different convergence scenarios in the two cases (insets), *i.e.*, the achievement of a phonon exceptional point (x~0, scenario ①) or a proper doublet inversion (x~1, scenario ②) – emphasized by an upward-curved arrow. A similar inversion (scenario ②) – emphasized by a downward-curved arrow – is observed for the Cd-Te doublet at x~0, that distinguishes between dominant/matrix-like TO^{Cd}_{Cd-Te} vibrations (regrouped by an oval) and minor/localized TO^{Zn}_{Cd-Te} vibrations near the Zn-trio (dotted arrow).

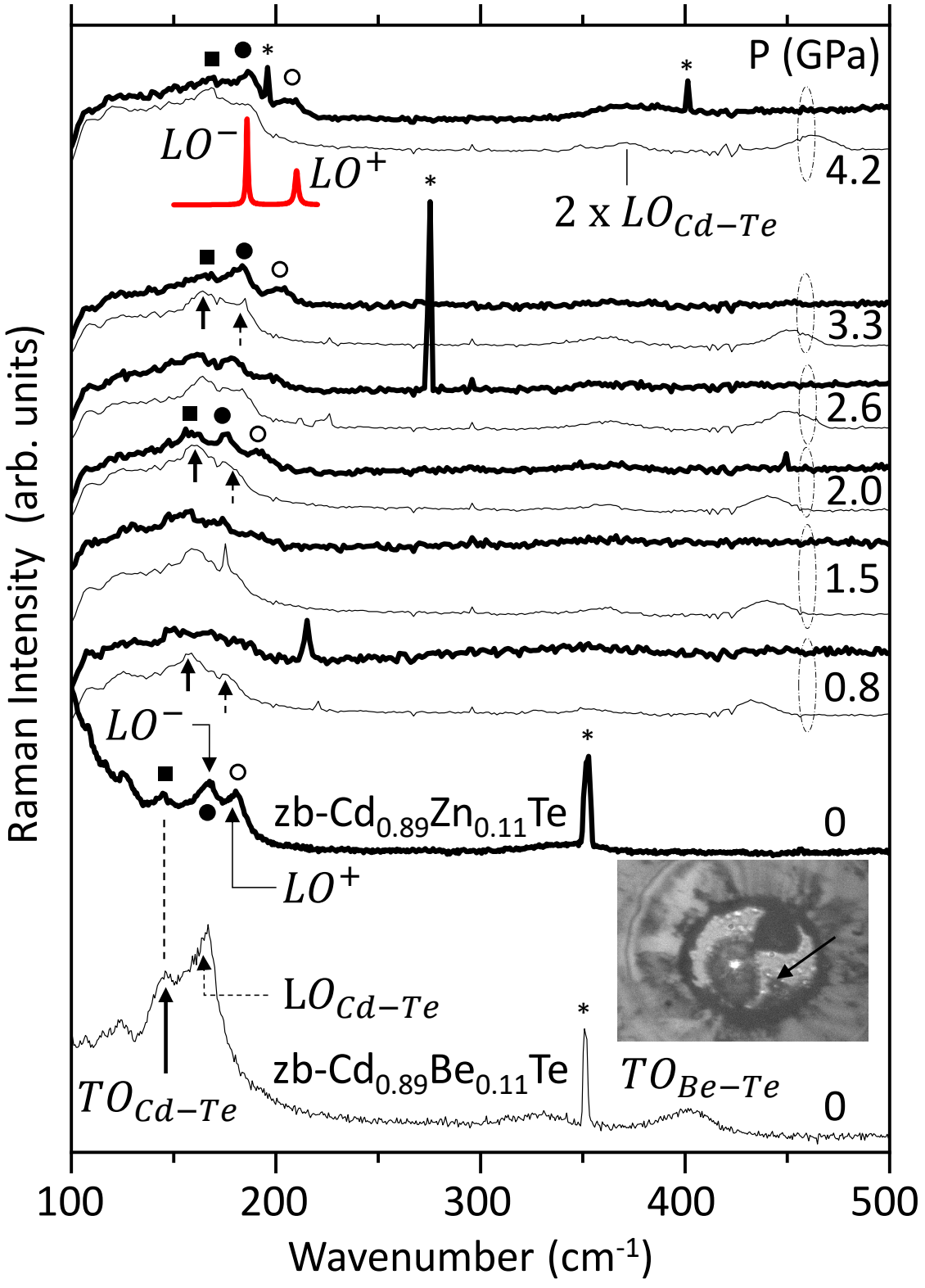

Fig. S6: **High-pressure $Cd_{0.89}Zn_{0.11}Te$ and $Cd_{0.89}Be_{0.11}Te$ Raman spectra**. High-pressure Raman spectra taken in the upstroke across the zincblende phases of $Cd_{0.89}Zn_{0.11}Te$ (thick curves) and $Cd_{0.89}Be_{0.11}Te$ (thin curves). The theoretical Raman signal due to the coupled LO^- (●) and LO^+ (○) modes of $Cd_{0.89}Zn_{0.11}Te$ at maximum pressure (thick-red curve) completes similar theoretical insights given at lower pressures in Fig. 3c/d. The TO_{Cd-Te} (■) is indicated, for reference purpose. The stars mark plasma lines. Inset: post-downstroke photograph of the clear/transparent $Cd_{0.89}Zn_{0.11}Te$ and dark/absorbing $Cd_{0.89}Be_{0.11}Te$ samples stowed together with the ruby (pointed by an arrow) used for pressure calibration. A spotlight is generated by the laser beam at the impact spot on the sample surface.

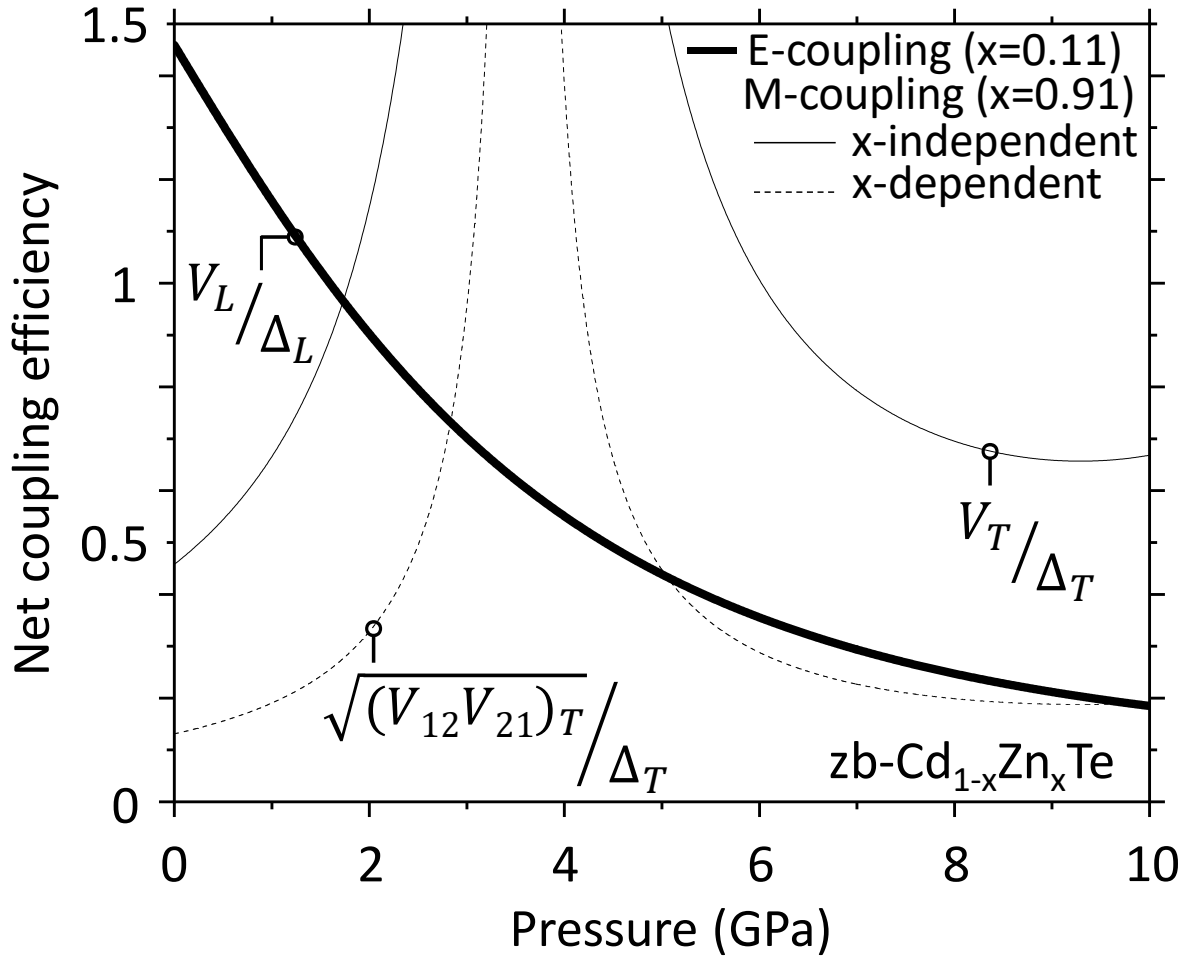

335

336 **Fig. S7**: **$Cd_{1-x}Zn_xTe$ TO-mechanical (x~0.9) vs. LO-electrical (x~0.1) net coupling efficiencies vs. pressure.** Net
337 efficiencies of the electrical (E) LO (L) coupling (thick curve, x=0.11) and mechanical (M) TO (T) coupling (thin
338 curves, x=0.91) in $Cd_{1-x}Zn_xTe$, as compromises between the strength of coupling (V) and the distance to the
339 resonance (Δ). The symmetric/x-independent (solid curve) and antisymmetric/x-dependent (dotted curve) TO
340 cases are distinguished. In the former TO-case V_{ij} is the asymmetrical mechanical coupling obtained by weighting
341 the mechanical coupling suffered by a given (u_i) oscillator by the fraction (x_j) of the other (u_j) oscillator in the
342 crystal.